applied sciences

MDPI

Article

Interface Characterization of Current-Perpendicular-to-Plane Spin Valves Based on Spin Gapless Semiconductor Mn_2CoAl

Ming-Sheng Wei, Zhou Cui, Xin Ruan, Qi-Wen Zhou, Xiao-Yi Fu, Zhen-Yan Liu, Qian-Ya Ma and Yu Feng *

School of Physics and Electronic Engineering, Jiangsu Normal University, Xuzhou 221116, China; weims@jsnu.edu.cn (M.-S.W.); cuizhoujsnu@163.com (Z.C.); ruanxinjsnu@163.com (X.R.); zhouqiwenjsnu@163.com (Q.-W.Z.); fuxiaoyijsnu@163.com (X.-Y.F.); liuzhenyanjsnu@163.com (Z.-Y.L.); maqianyajsnu@163.com (Q.-Y.M.)

* Correspondence: fengyu@jsnu.edu.cn; Tel.: +86-516-835-00485

Received: 19 July 2018; Accepted: 9 August 2018; Published: 10 August 2018

Featured Application: Current-perpendicular-to-plane spin valve based on spin gapless semiconductor Mn_2CoAl with MnCo termination possesses high value of magnetoresistance of 2886% and has a better application in a spintronics device.

Abstract: Employing the first-principles calculations within density functional theory (DFT) combined with the nonequilibrium Green's function, we investigated the interfacial electronic, magnetic, and spin transport properties of $Mn_2CoAl/Ag/Mn_2CoAl$ current-perpendicular-to-plane spin valves (CPP-SV). Due to the interface rehybridization, the magnetic moment of the interface atom gets enhanced. Further analysis on electronic structures reveals that owing to the interface states, the interface spin polarization is decreased. The largest interface spin polarization (ISP) of 78% belongs to the $MnCo^{T}$-terminated interface, and the ISP of the $MnMn^{T1}$-terminated interface is also as high as 45%. The transmission curves of $Mn_2CoAl/Ag/Mn_2CoAl$ reveal that the transmission coefficient at the Fermi level in the majority spin channel is much higher than that in the minority spin channel. Furthermore, the calculated magnetoresistance (MR) ratio of the $MnCo^{T}$-terminated interface reaches up to 2886%, while that of the $MnMn^{T1}$-terminated interface is only 330%. Therefore, $Mn_2CoAl/Ag/Mn_2CoAl$ CPP-SV with an MnCo-terminated interface structure has a better application in a spintronics device.

Keywords: Heusler alloy; spin gapless semiconductor; electronic structure; spin transport

1. Introduction

The current-perpendicular-to-plane spin valve (CPP-SV) is regarded as one of the most significant spintronics devices, and has great potential for spin transfer torque devices in spin random access memory and ultra-high-speed reading in magnetic read heads of hard disk drivers [1–4]. The generation and detection of highly polarized spin current is one of the foremost challenges of a CPP-SV. Half metallic Heusler alloys (HMHA) usually have a high Curie temperature (T_C) and their lattice constants are close to Ag and Cu. In addition, one spin band (majority spin) of HMHA exhibits metallic behavior, while the other spin band (minority spin) displays semiconductor behavior, and such a band structure could generate a high spin polarized current. Therefore, HMHA has been explored as an electrode of CPP-SV to achieve a high magnetoresistance (MR) ratio [5–11]. Takayashi et al. reported a large MR ratio of 74.8% at room temperature (RT) in CPP-SV using $Co_2MnGa_{0.25}Ge_{0.75}$ [12]. Sakuraba et al. demonstrated an MR ratio of 58% at RT and 184% at 30 K in $Co_2Fe_{0.4}Mn_{0.6}Si/Ag$

CPP-SV [13]. Moreover, a number of CPP-SVs employing a Heusler alloy as the spin injector, such as Co_2MnSi/Ag, $Co_2FeAl_{0.5}Si_{0.5}/Ag$, and $Co_2FeGa_{0.5}Ge_{0.5}/Ag$, also obtained high MR ratios [14,15]. More recently, the Hg_2CuTi type Heusler alloy Mn_2CoAl has been demonstrated to be one of the spin gapless semiconductors (SGS) from theoretical calculation combined with experimental work [16–26]. The minority spin band of Mn_2CoAl has an energy gap around the Fermi level, while the top of the valence band and the bottom of the conduction band touch at the Fermi level (see Figure 1). The special band structure allows the holes and electrons to be spin polarized simultaneously. Mn_2CoAl has attracted much attention and it is considered to possess great potential for spintronics. Since the MR ratio of spin valves based on a Heusler alloy severely depends on its interface properties, and in order to explore outstanding candidates for CPP-SV, we study the interface magnetism, electronic structure, and spin transport properties of $Mn_2CoAl/Ag/Mn_2CoAl$ CPP-SV.

There are two ideal terminations along the (0 0 1) direction in a Heusler alloy Mn_2CoAl: MnCo and MnAl. Besides, there are two ways to connect a Heusler alloy with an Ag spacer, one of which is where atoms from the Heusler alloy sit on top of Ag atoms, which is noted as $MnCo^T$ and $MnAl^T$. The other way is where atoms from the Heusler alloy locate in the bridge site between Ag atoms, which is noted as $MnCo^B$ and $MnAl^B$. In addition, according to previous works, a pure Mn-modified artificial termination could improve the spin polarization [27,28], so MnMn terminations are also considered. When interface Co atoms in $MnCo^T$ and $MnCo^B$ are replaced by Mn atoms, $MnMn^{T1}$ and $MnMn^{B1}$ are built, respectively. Similarly, when interface Al atoms in $MnAl^T$ and $MnAl^B$ are substituted with Mn atoms, $MnMn^{T2}$ and $MnMn^{B2}$ are built, respectively. Various interface structures of $Mn_2CoAl/Ag/Mn_2CoAl$ CPP-SV are exhibited in Figure 2.

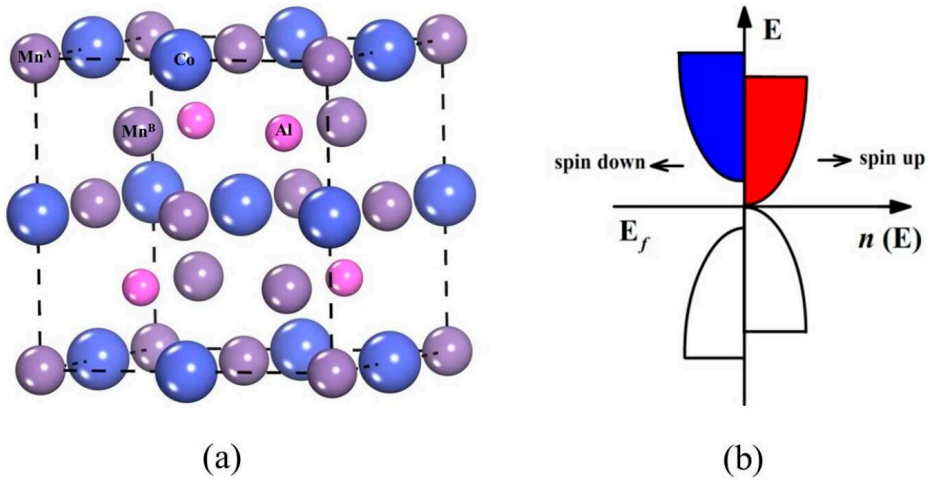

Figure 1. (**a**) Schematic representation of Mn_2CoAl bulk structure. The schematic density of states of n (E) as a function of energy E is shown for (**b**) a spin gapless semiconductor. The occupied states are indicated by filled areas. Arrows indicate the majority and minority states.

2. Calculation Methods

The structure optimization, electronic, and magnetic properties are calculated by utilizing the Vienna ab initio Simulation Package (VASP) based on density functional theory (DFT) within generalized gradient approximation (GGA) [29]. We make use of projector-augmental wave (PAW) [30] pseudopotential to deal with the electron-iron interaction, and the Mn ($3d^5 4s^2$), Co ($3d^7 4s^2$), Al ($3s^2 3p^1$), and Ag ($4d^{10} 5s^1$) are selected as valence-electron configurations. The mesh of special k-points in the Brillouin zone is set to $7 \times 7 \times 1$ and the SCF convergence criterion of 10^{-6} eV is applied. The cutoff energy is taken to be 500 eV. The optimized Ag and Mn_2CoAl bulks are cleaved along the Miller indices (0 0 1) crystal direction, and we chose 13 Mn_2CoAl layers as the electrode and nine Ag layers as the spacer layer to compose the $Mn_2CoAl/Ag/Mn_2CoAl$ heterojunction. The in-plane

lattice parameter is fixed to 4.1 Å, which corresponds to $1/\sqrt{2}$ of the experimental lattice constant of Mn_2CoAl bulk (5.798 Å [20]), and such a value is very close to the lattice constant of Ag. Therefore, the lattice mismatch between the Mn_2CoAl electrode and Ag is very small. The spin-dependent transport properties calculations are based on a state-of-the-art technique where DFT is combined with the Keldysh nonequilibrium Green's function (NEGF) theory, as implemented in the Nanodcal package [31,32].

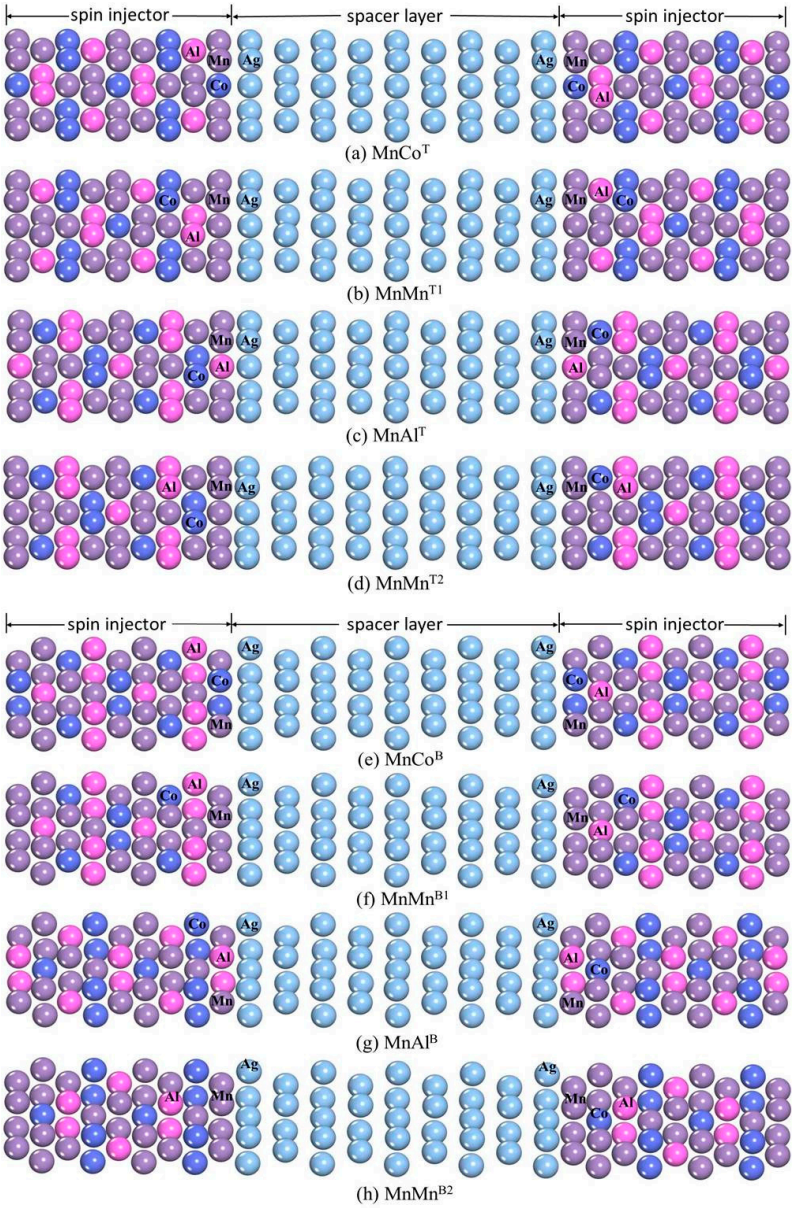

Figure 2. Various atomic terminations of the $Mn_2CoAl/Ag/Mn_2CoAl$ (001) interface.

3. Result and Discussion

The displacements of interface atoms in various $Mn_2CoAl/Ag/Mn_2CoAl$ structures are measured and exhibited in Figure 3. L1 and L2 indicate the interface and subinterface, respectively. It can be seen that the interfacial Mn^{A} atom has an obvious outward extension in MnCo^{B}, MnCo^{T}, MnMn^{T1}, and MnMn^{B1} structures, revealing that the interface Mn atom prefers to bond with the interface atom from the spacer layer, and such behavior is also reported in previous theoretical and experimental studies [33,34]. As for the interfacial Mn^{B} atom, it slightly stretches outward in MnMn^{T2} and MnMn^{B2},

and keeps its ideal position in $MnAl^T$, while it even shrinks inward in $MnAl^B$, showing that its bonding ability is weaker than interfacial Mn^A. The interface Co atom has a slight outward movement, and when the $MnMn^{T1}$ and $MnMn^{B1}$-terminated interface are respectively formed by substituting interface Co with the Mn atom, such an outward action is enhanced. Besides, for various different structures, the outward movement of the subinterface atom is very small, and the position of the next subinterface atom is nearly unchanged, so their behaviors are extremely similar to the bulk (not shown in Figure 3).

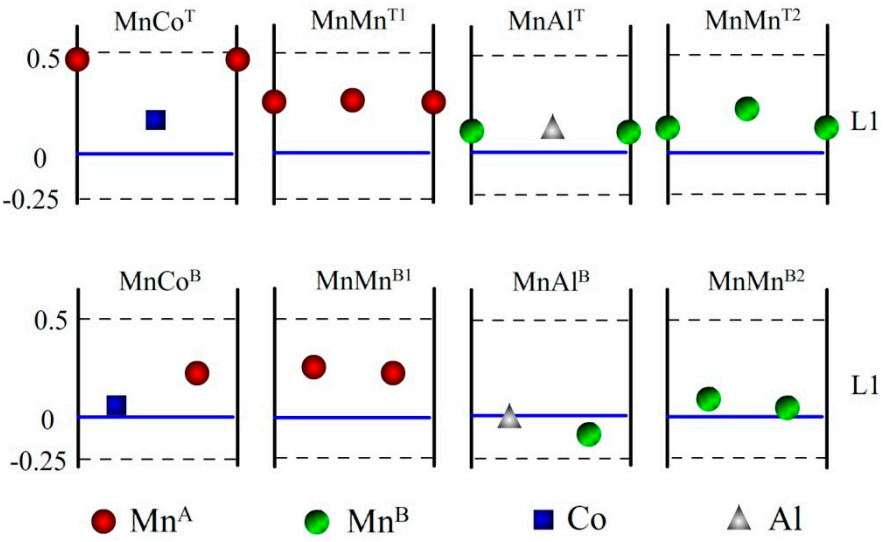

Figure 3. The relaxed atomic positions in various terminations. L1 and L2 indicate the interface and subinterface, respectively.

The interface free energy (γ) versus atomic chemical potentials is calculated in order to determine the interface stability. As was mentioned in Ref. [34], the γ can be expressed as

$$\gamma = \frac{1}{2A}\left[G - \sum_i \mu_i N_i\right] \quad (1)$$

where A is the interface area of a supercell, G stands for the Gibbs free energy of the slab; and μ_i and N_i are the chemical potential and the number of the ith atom, respectively. The relationship among the interdependent chemical potentials can be expressed as $2\mu_{Mn} + \mu_{Co} + \mu_{Al} = G_{bulk}$. Besides, the highest values of μ_{Co} and μ_{Mn} are $\mu_{Co} = G_{Co}$ and $\mu_{Mn} = G_{Mn}$, where G_{Co} and G_{Mn} are Gibbs free energies of the Co and Mn bulk, respectively. Besides, due to the reason that 2Mn + CoAl = Mn_2CoAl and Co + Mn_2Al = Mn_2CoAl, the lowest values of μ_{Co} and μ_{Mn} are

$$\mu_{Mn} = \frac{1}{2}[G_{bulk} - G_{CoAl}],\ \mu_{Co} = \frac{1}{2}\left[G_{bulk} - G_{Mn_2Al}\right] \quad (2)$$

In Figure 4, the $MnMn^{T1}$ and $MnMn^{B1}$ always stay in the thermodynamic accessible region (TAR) and occupy the maximum area. As μ_{Mn} and μ_{Co} increase, $MnMn^{T2}$, $MnMn^{B2}$, $MnCo^T$, and $MnCo^B$ are included in the TAR, revealing that these interfaces could be stable under the condition of Mn rich and Co rich. In addition, $MnMn^{B2}$ enters into the TAR under the condition of $\mu_{Co} = -0.702$ Ryd and $\mu_{Mn} = -0.523$ Ryd, while $MnMn^{T2}$ appears in the TAR when $\mu_{Co} = -0.702$ Ryd and $\mu_{Mn} = -0.694$ Ryd, indicating that the formation of a stable $MnMn^{T2}$ needs a richer Mn condition than $MnMn^{B2}$. In the case of $MnCo^B$, it enters into the TAR when μ_{Co} and μ_{Mn} respectively increase to -0.672 Ryd and -0.477 Ryd, while $MnCo^T$ appears in the TAR when $\mu_{Co} = -0.68$ Ryd and $\mu_{Mn} = -0.547$ Ryd. Therefore, it could be deduced that the MnCo terminated interface can be more easily obtained in a bridge-type

structure than in a top-type structure. However, as for MnAl terminated interfaces, they are excluded from the TAR in both top-type and bridge-type structures.

The atom-resolved spin magnetic moments (AMMs) in the first three layers are plotted in Figure 5. In the Mn_2CoAl bulk, each atom locates at a tetrahedral symmetry position, and each Co and Mn^A atom has four Al and four Mn^B as the nearest neighbors. While in the $Mn_2CoAl/Ag/Mn_2CoAl$ heterostructures, an Ag atom takes the place of half of the nearest neighbors of the interface atom, reducing atomic coordination numbers at the interface. As a result, it breaks the periodic crystal field at the interface and the localization of the *d*-electron atom at the interface is enhanced. Therefore, AMMs of interface atoms are strengthened in various structures, and are larger than their corresponding bulk values. Besides, the relative distance between magnetic atoms could also affect the value of AMM. The maximum outward extension belongs to the interface Mn atom in the $MnCo^T$ structure, and it results in reduced hybridization and strengthened localization. Therefore, its AMM rises up to the highest value of 3.73 μ_B. The interface Mn atom in $MnMn^{B1}$ has a lower AMM than in $MnCo^B$, although they have a similar outward movement. This could be ascribed to the fact that the interface of $MnMn^{B1}$ is completely occupied by Mn atoms, and the interaction between Mn atoms is stronger than that between Co and Mn atoms. Such an explanation is also applied to the interface Mn atom in $MnAl^T$ and $MnMn^{T2}$, as well as $MnAl^B$ and $MnMn^{B2}$.

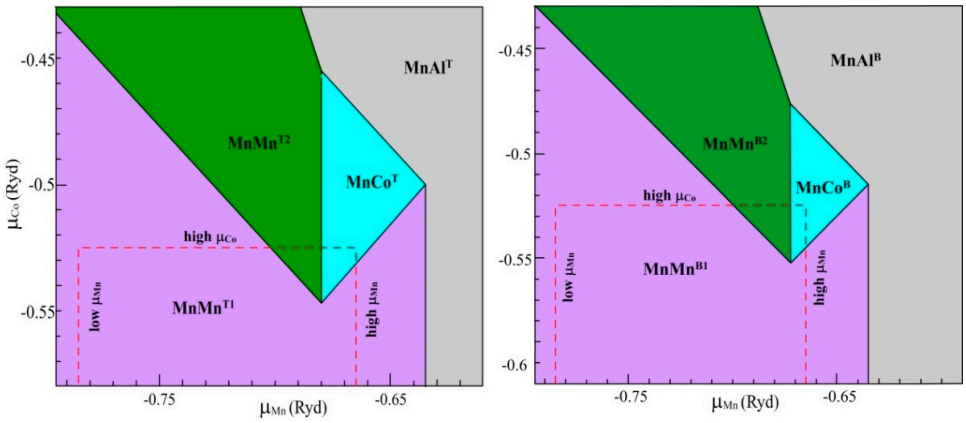

Figure 4. The calculated phase diagram of the $Mn_2CoAl/Ag/Mn_2CoAl$ (001) interface. The dashed lines denote the thermodynamically accessible region.

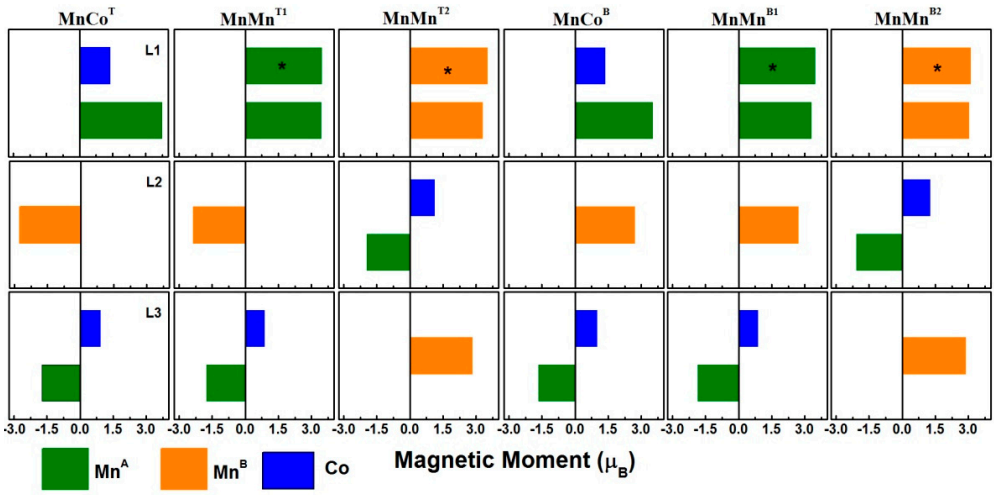

Figure 5. Atom-resolved spin magnetic moment of magnetic atoms of various terminations. L1, L2, and L3 indicate the interface, subinterface, and next subinterface, respectively. The region with '*' stands for the replaced atom.

Owing to the fact that subinterface atoms have small displacement, and the atom at the next subinterface maintains its position, AMMs of the subinterface and the next subinterface atoms could be compared to corresponding values in the bulk, revealing that atoms at deeper layers receive a minor interface effect. AMM of the Al atom presents negative values due to the fact that the *sp*-atom has a function of a bridge between local *d*-electron atoms according to the RKKY exchange model.

Spin transportation of a spintronics device severely depends on interface spin polarization (ISP), which can be written as $(D_\uparrow - D_\downarrow)/(D_\uparrow + D_\downarrow)$, where the $D_\uparrow$ and $D_\downarrow$ respectively represent the majority spin density of states and minority spin density of states. First, we calculate the total density of states (DOS). It can be seen from Figure 6 that interface half-metallicity is not detected in various structures. The $MnCo^T$ interface displays the highest ISP of 78%, and the ISP of $MnMn^{T1}$ also exhibits a value as high as 45%; while the ISP of $MnMn^{T2}$, $MnCo^T$, and $MnMn^{B1}$ are only 26%, 33%, and 32%, respectively. The ISP of $MnMn^{B2}$ even descends to a poor value of 10%. Hence, it reveals that with different $Co_2MnSi/GaAs$ and $CoFeMnSi/GaAs$ heterojunctions [27,35], the interface containing the pure Mn atom in Mn_2CoAl/Ag spin valves could not improve the ISP.

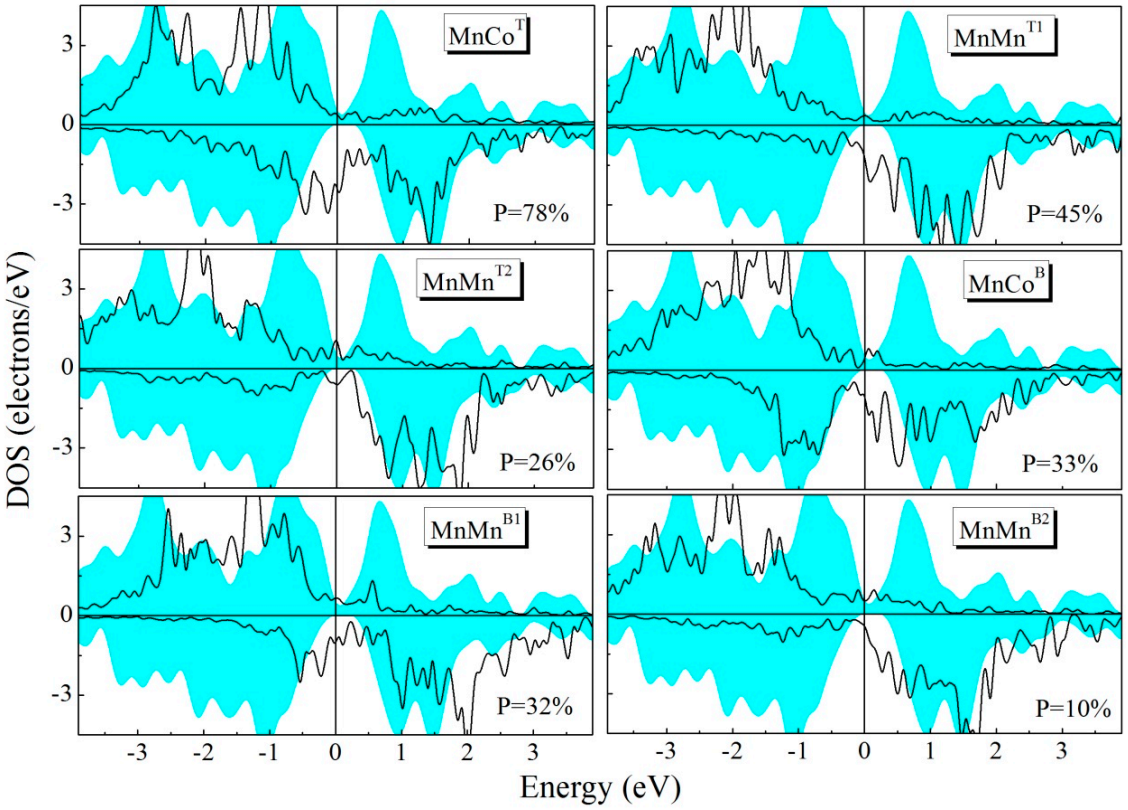

Figure 6. The total density of states (DOS) of various structures. The shadow region indicates the DOS of the Mn_2CoAl bulk. P stands for spin polarization.

Due to the reason that $MnCo^T$ and $MnMn^{T1}$ structures possess a high ISP, the project density of states (PDOS) in the interface, subinterface, and the next subinterface of these two terminated structures are further investigated and displayed in Figure 7. As for the interface magnetic atom, its majority spin band shifts to the lower energy region, while the minority spin band moves towards the higher energy region. Therefore, the exchange splitting is increased and magnetic moments are increased owing to the truncated periodic crystal field at the interface. The Mn^A atom in Mn_2CoAl bulk displays reverse splitting, which leads to its negative value of magnetic moment, while it converts to normal splitting at the interface, and its magnetic moment obtains a positive value. Quite the opposite, the normal splitting of the Mn^B atom in the bulk shifts to reverse splitting at the subinterface of $MnCo^T$

and $MnMn^{T1}$ structures. It indicates that the antiferromagnetic interaction of Mn^{A} in bulk turns to a ferromagnetic interaction when it at the interface, while the ferromagnetic coupling of bulk Mn^{B} converts to antiferromagnetic coupling when at the subinterface. Besides, some polarized peaks which have a *d*-orbital characteristic appear in the minority spin energy gap at the interface, and the energy of these peaks decreases in the second layer and finally vanishes in the third layer. Therefore, these polarized peaks are considered to be interface states, and they are responsible for the destruction of interface half-metallicity. In addition, it can be seen that the PDOSs of atoms at the third layer are very similar to their features in bulk, revealing that the electronic structures of the deeper layer receive a minor influence of the interface effect.

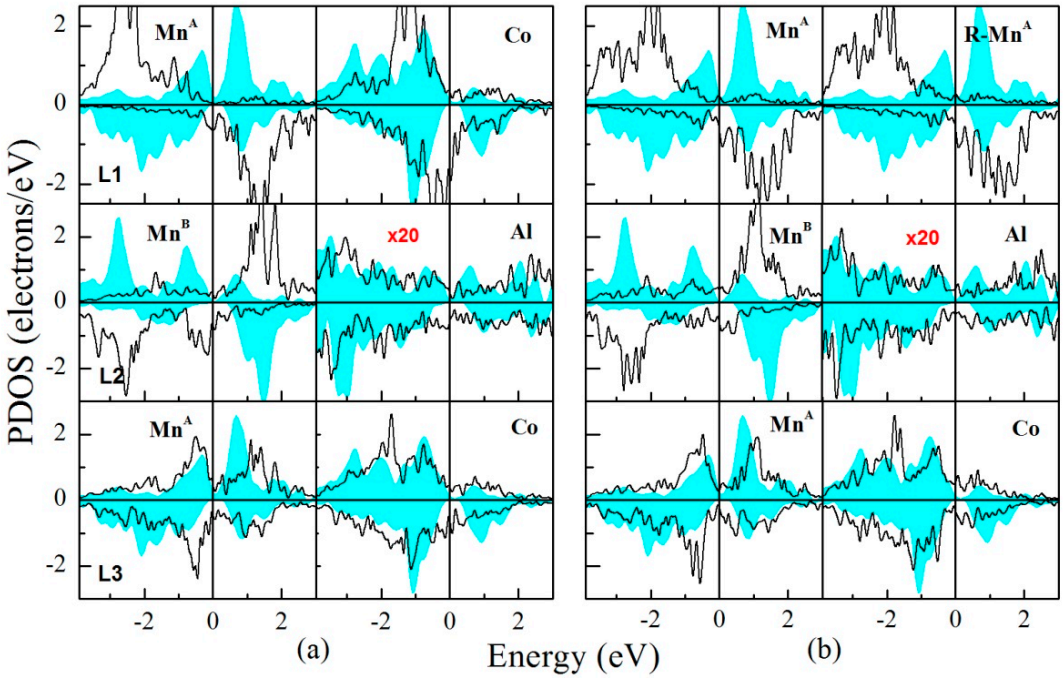

Figure 7. The partial density of states (PDOS) of (**a**) $MnCo^{T}$- and (**b**) $MnMn^{T1}$-terminated structures. The shadow region indicates atomic PDOS of the bulk. L1, L2, and L3 indicate the interface, subinterface, and next subinterface, respectively.

Among various investigated structures, due to the reason that the ISP of the $MnCo^{T}$-terminated and $MnMn^{T1}$-terminated interface reaches up to 78% and 45%, respectively; the transport properties of the $Mn_2CoAl/Ag/Mn_2CoAl$ spin valve with an $MnCo^{T}$-terminated and $MnMn^{T1}$-terminated interface have been calculated. The energy- and spin-resolved transmission coefficient $T^{\sigma}(E)$ is defined as

$$T^{\sigma}(E) = \frac{1}{n^2}\int d^2k_{//}T^{\sigma}(\vec{k}_{//}, E) \tag{3}$$

where n^2 represents the number of sampling points in the two-dimensional Brillouin zone (2-D BZ), and σ is the spin direction. The transmission coefficients of the $Mn_2CoAl/Ag/Mn_2CoAl$ junction with an $MnCo^{T}$-terminated and $MnMn^{T1}$-terminated interface at equilibrium are calculated and presented in Figure 8, and the Fermi level has an energy of zero. When magnetic moments of two Mn_2CoAl electrode layers are in a parallel configuration (PC), the transmission coefficient curve of the majority spin channel is totally different to that of the minority spin channel. For the $MnCo^{T}$-terminated structure, the value of the transmission coefficient of the majority spin channel at Fermi level $T_{PC}^{maj}(E_f)$ is 0.00663, and that of the minority spin channel at Fermi level $T_{PC}^{\min}(E_f)$ is almost zero. For the $MnMn^{T1}$-terminated structure, $T_{PC}^{maj}(E_f)$ is 0.0038 and $T_{PC}^{\min}(E_f)$ is also close to zero. When the magnetic moments of two Mn_2CoAl electrode layers are in an anti-parallel configuration (APC),

due to the reason that our $Mn_2CoAl/Ag/Mn_2CoAl$ spin valve model is geometrically symmetric with respect to the middle plane of the center scattering region, the transmission coefficient curve of the spin up channel is exactly the same as that of the spin down channel. For the $MnCo^T$-terminated structure, the value of the transmission coefficient of the majority spin channel and minority spin channel at the Fermi level is $T^{maj}_{APC}(E_f) = T^{\min}_{APC}(E_f) = 0.111 \times 10^{-3}$. For the $MnMn^{T1}$-terminated structure, $T^{maj}_{APC}(E_f) = T^{\min}_{APC}(E_f) = 0.442 \times 10^{-3}$.

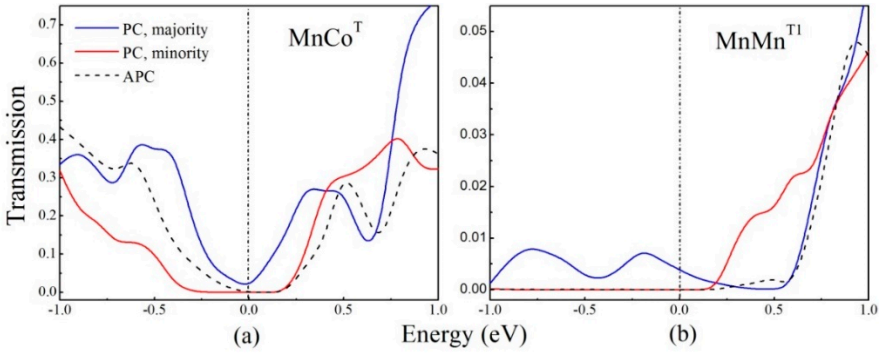

Figure 8. Transmission coefficient versus electron energy in PC (parallel configuration) and APC (anti-parallel configuration) of the $Mn_2CoAl/Ag/Mn_2CoAl$ CPP-SV at equilibrium; (**a**) The structure with $MnCo^T$-termination; (**b**) The structure with $MnMn^{T1}$-termination.

The magnetoresistance (MR) ratio of $Mn_2CoAl/Ag/Mn_2CoAl$ CPP-SV with an $MnCo^T$-terminated and $MnMn^{T1}$-terminated interface is also calculated by:

$$MR = \left| \frac{G_{pc} - G_{APC}}{\min(G_{pc}, G_{APC})} \right| \times 100\% \quad (4)$$

where G_{pc} and G_{Apc} are conductance at the Fermi level in PC and APC, respectively, where $G_{PC} = T^{maj}_{PC} + T^{\min}_{PC}$ and $G_{APC} = T^{maj}_{APC} + T^{\min}_{APC}$. According to the calculated values in Figure 8, the MR ratio of the $MnCo^T$-terminated structure is as high as 2886%, while that of the $MnMn^{T1}$-terminated structure is only about 330%. Our calculated results indicate that the $Mn_2CoAl/Ag/Mn_2CoAl$ spin valve with the $MnCo^T$-terminated interface is a high-performance spintronics device. Furthermore, the 2-D BZ transmission coefficients at the Fermi level as a function of k_x and k_y, which are perpendicular to the transport direction (z axis), have been calculated at equilibrium. The contour plots of the $\vec{k}_{//}$ dependence of the spin up and spin down transmission coefficients in PC and APC have been mapped in Figure 9. It can be seen that the density of dark-red spots in Figure 9a is much higher than that in Figure 9b, indicating that the majority spin electrons in PC have larger transmission probabilities than minority spin electrons, and it is consistent with the calculated transmission curves exhibited in Figure 8. In addition, the contour plots of the majority spin transmission coefficient in APC are exactly the same as those of the minority spin transmission coefficient, and rare *hot spots* exist in Figure 9c,d, indicating that the transmissions of both majority spin and minority spin channels in APC have been suppressed.

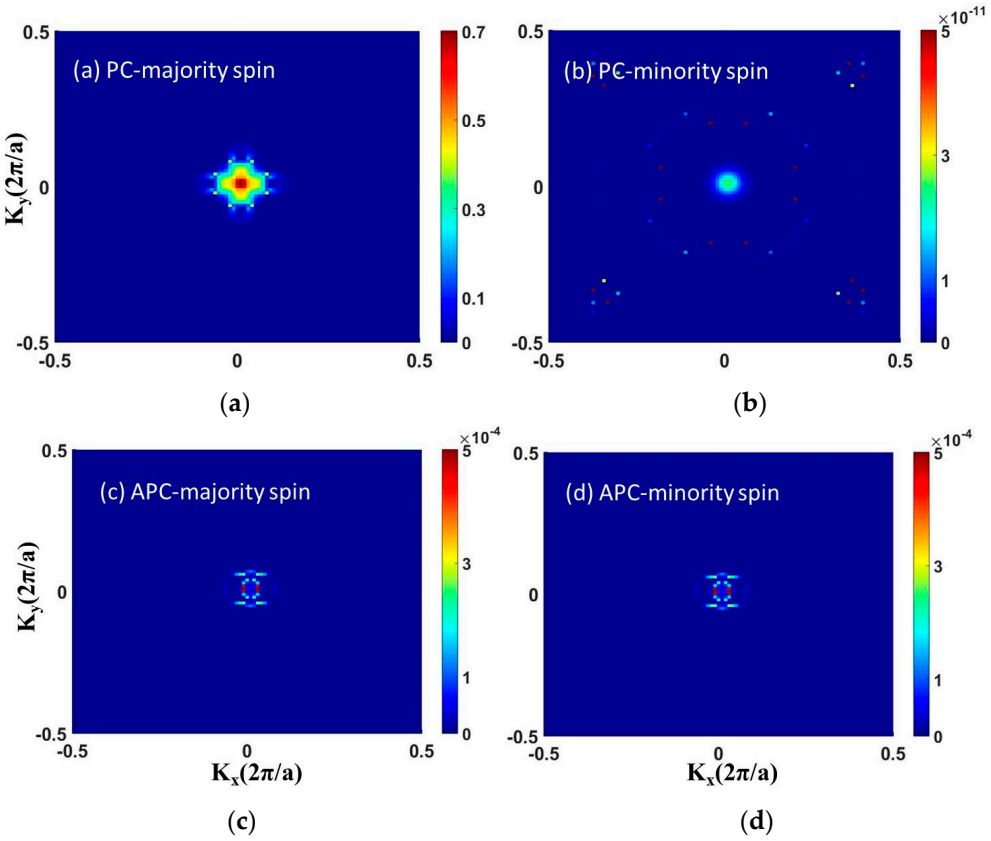

Figure 9. The $k_{//}$-resolved transmission coefficients of the $MnCo^T$-terminated structure at the Fermi level $E = E_f$. (**a**) Majoirty spin in PC; (**b**) minority spin in PC; (**c**) majority spin in APC; (**d**) minority spin in APC.

4. Conclusions

Combining the first-principles calculations within density functional theory (DFT) with nonequilibrium Green's function, we investigated the interface magnetism and electronic structures of $Mn_2CoAl/Ag/Mn_2CoAl$ CPP-SV. Our calculations reveal that due to the reason that crystal symmetry at the interface is broken, the rehybridization leading to the AMMs of atoms at the interface becomes enhanced. Moreover, analyses of electronic structures reveal that owing to the interface states, the interface half-metallicity is destroyed. The $MnCo^T$-terminated interface preserves the highest ISP of 78%, and the $MnMn^{T1}$-terminated interface also has a high ISP of 45%. The transmission curves reveal that the transmission coefficient at the Fermi level in the majority spin channel is much higher than that in the minority spin channel. Furthermore, the calculated magnetoresistance (MR) ratio of the $MnCo^T$-terminated interface reaches up to 2886%, while that of the $MnMn^{T1}$-terminated interface is only 330%. Therefore, $Mn_2CoAl/Ag/Mn_2CoAl$ CPP-SV with an $MnCo^T$-terminated interface structure has a better application in a spintronics device.

Author Contributions: Conceptualization, Q.-Y.M.; Methodology, X.-Y.F.; Software, X.R.; Data Curation, Z.-Y.L.; Writing-Original Draft Preparation, Z.C. and X.R.; Writing-Review & Editing, M.-S.W.; Supervision, Y.F.

Funding: This research was funded by [National Natural Science Foundation of China] grant number [11747114], and by [Doctor Foundation of Jiangsu Normal University] grant number [17XLR046 and 16XLR022], and by [Xuzhou Technology Plan Project] grant number [KC16SQ179].

Conflicts of Interest: The author declares no conflict of interest.

References

1. Wolf, S.A.; Awschalom, D.D.; Buhrman, R.A.; Daughton, J.M.; von Molnár, S.; Roukes, M.L.; Chtchelkanova, A.Y.; Treger, D.M. Spintronics: A spin-based electronics vision for the future. *Science* **2001**, *294*, 1488–1495. [CrossRef] [PubMed]
2. Li, X.; Yang, J. First-principles design of spintronics materials. *Natl. Sci. Rev.* **2016**, *3*, 365–381. [CrossRef]
3. Nakatani, T.M.; Furubayashi, T.; Kasai, S.; Sukegawa, H.; Takahashi, Y.K.; Mitani, S.; Hono, K. Bulk and interfacial scatterings in current-perpendicular-to-plane giant magnetoresistance with $Co_2Fe(Al_{0.5}Si_{0.5})$ Heusler alloy layers and Ag spacer. *Appl. Phys. Lett.* **2010**, *96*, 212501. [CrossRef]
4. Childress, J.R.; Carey, M.J.; Cyrille, M.C.; Carey, K.; Smith, N.; Katine, J.A.; Boone, T.D.; Driskill-Smith, A.A.G.; Maat, S.; Mackay, K.; et al. Fabrication and recording study of all-metal dual-spin-valve CPP read heads. *IEEE Trans. Magn.* **2006**, *42*, 2444–2446. [CrossRef]
5. Graf, T.; Felser, C.; Parkin, S.S.P. Simple rules for the understanding of Heusler compounds. *Prog. Solid State Chem.* **2011**, *39*, 1–50. [CrossRef]
6. Felser, C.; Fecher, G.H. (Eds.) *Spintronics*; Springer: Berlin, Germany, 2013.
7. Galanakis, I.; Dederichs, P. (Eds.) Half-metallicity and Slater-Pauling behavior in the ferromagnetic Heusler alloys. In *Half-Metallic Alloys*; Springer: Berlin, Germany, 2005.
8. Feng, Y.; Chen, H.; Yuan, H.K.; Zhou, Y.; Chen, X. The effect of disorder on electronic and magnetic properties of quaternary Heusler alloy CoFeMnSi with LiMgPbSb-type structure. *J. Magn. Magn. Mater.* **2015**, *378*, 7–15. [CrossRef]
9. Wang, X.T.; Cheng, Z.; Liu, G.; Dai, X.; Rabah, K.; Wang, L.; Bouhemadou, A. Rare earth-based quaternary Heusler compounds MCoVZ (M = Lu, Y; Z = Si, Ge) with tunable band characteristics for potential spintroic applications. *IUCrJ* **2017**, *4*, 758–768. [CrossRef] [PubMed]
10. Jourdan, M.; Minár, J.; Braum, J.; Kronenerg, A.; Chadov, S.; Balke, B.; Gloskovskii, A.; Kolbe, M.; Elmers, H.J.; Schönhense, G.; et al. Direct observation of half-metallicity in the Heusler compound Co_2MnSi. *Nat. Commun.* **2014**, *5*, 3974. [CrossRef] [PubMed]
11. Galanakis, I.; Dederichs, P.H.; Papanikolaou, N. Slater-Pauling behavior and origin of the half-metallicity of the full-Heusler alloys. *Phys. Rev. B* **2002**, *66*, 174429. [CrossRef]
12. Takahashi, Y.K.; Hase, N.; Kodzuka, M.; Itoh, A.; Koganezawa, T.; Furubayashi, T.; Li, S.; Varaprasad, B.S.D.C.S.; Ohkubo, T.; Hono, K. Structure and magnetoresistance of current-perpendicular-to-plane pseudo spin valves using $Co_2Mn(Ga_{0.25}Ge_{0.75})$ Heusler alloy. *J. Appl. Phys.* **2013**, *113*, 223901. [CrossRef]
13. Sakuraba, Y.; Ueda, M.; Miura, Y.; Sato, K.; Bosu, S.; Saito, K.; Shirai, M.; Konno, T.; Takanashi, K. Extensive study of giant magnetoresistance properties in half-metallic Co_2(Fe,Mn)Si-based devices. *J. Appl. Phys. Lett.* **2012**, *101*, 252408. [CrossRef]
14. Sakuraba, Y.; Izumi, K.; Miura, Y.; Futasukawa, K.; Iwase, T.; Bosu, S.; Saito, K.; Abe, K.; Shirai, M.; Takanashi, K. Mechanism of large magnetoresistance in $Co_2MnSi/Ag/Co_2MnSi$ devices with current perpendicular to the plane. *Phys. Rev. B* **2010**, *82*, 094444. [CrossRef]
15. Li, S.; Takahashi, Y.K.; Furubayashi, T.; Hono, K. Enhancement of giant magnetoresistance by $L2_1$ ordering in $Co_2Fe(Ge_{0.5}Ga_{0.5})$ Heusler alloy current-perpendicular-to-plane pseudo spin valves. *Appl. Phys. Lett.* **2013**, *103*, 042405. [CrossRef]
16. Skaftouros, S.; Özdoğan, K.; Şaşioğlu, E.; Galanakis, I. Generalized Slater-Pauling rule for the inverse Heusler compounds. *Phys. Rev. B* **2013**, *87*, 024420. [CrossRef]
17. Feng, L.; Tang, C.; Wang, S.; He, W. Half-metallic full-Heusler compound Ti_2NiAl: A first-principles study. *J. Alloy. Compd.* **2011**, *509*, 5187–5189.
18. Feng, Y.; Wu, B.; Yuan, H.K.; Kuang, A.L.; Chen, H. Magnetism and half-metallicity in bulk and (1 0 0) surface of Heusler alloy Ti_2CoAl with Hg_2CuTi-type structure. *J. Alloy. Compd.* **2013**, *557*, 202–208. [CrossRef]
19. Jakobsson, A.; Mavropoulos, P.; Şaşioğlu, E.; Blügel, S.; Ležaić, M.; Sanyal, B.; Galanakis, I. First-principles calculations of exchange interactions, spin waves, and temperature dependence of magnetization in inverse-Heusler-based spin gapless semiconductors. *Phys. Rev. B* **2015**, *91*, 174439. [CrossRef]
20. Ouardi, S.; Fecher, G.H.; Felser, C.; Kübler, J. Realization of Spin Gapless Semiconductors: The Heusler Compound Mn_2CoAl. *Phys. Rev. Lett.* **2013**, *110*, 100401. [CrossRef] [PubMed]
21. Galanakis, I.; Özdoğan, K.; Şaşıoğlu, E.; Blügel, S. Conditions for spin-gapless semiconducting behavior in Mn_2CoAl inverse Heusler compound. *J. Appl. Phys.* **2014**, *115*, 093908. [CrossRef]

22. Jamer, M.E.; Assaf, B.A.; Devakul, T. Magnetic and transport properties of Mn_2CoAl oriented films. *Appl. Phys. Lett.* **2013**, *103*, 142403. [CrossRef]
23. Xu, G.Z.; Du, Y.; Zhang, X.M.; Zhang, H.G.; Liu, E.K.; Wang, W.H.; Wu, G.H. Magneto-transport properties of oriented Mn_2CoAl films sputtered on thermally oxidized Si substrates. *Appl. Phys. Lett.* **2014**, *104*, 242408. [CrossRef]
24. Skaftouros, S.; Özdoğan, K.; Şaşioğlu, E.; Galanakis, I. Search for spin gapless semiconductors: The case of inverse Heusler compounds. *Appl. Phys. Lett.* **2013**, *102*, 022402. [CrossRef]
25. Wang, X.L. Proposal for a new class of materials: Spin gapless semiconductors. *Phys. Rev. Lett.* **2008**, *100*, 156404. [CrossRef] [PubMed]
26. Feng, Y.; Zhou, T.; Chen, X.; Yuan, H.K.; Chen, H. Thermodynamic stability, magnetism and half metallicity of Mn_2CoAl/GaAs (0 0 1) interface. *J. Phys. D Appl. Phys.* **2015**, *48*, 285302. [CrossRef]
27. Zarei, S.; Hashemifar, S.J.; Akbarzadeh, H.; Hafari, H.J. Half-metallicity at the Heusler alloy $Co_2Cr_{0.5}Fe_{0.5}Al$ (001) surface and its interface with GaAs (001). *Phys. Condens. Matter* **2009**, *21*, 055002. [CrossRef] [PubMed]
28. Perdew, J.P.; Burke, K.; Ernzerhof, M. Generalized gradient approximation made simple. *Phys. Rev. Lett.* **1996**, *77*, 3865–3868. [CrossRef] [PubMed]
29. Blöchl, P.E. Projector augmented-wave method. *Phys. Rev. B* **1994**, *50*, 17953. [CrossRef]
30. Ghader, N.; Hashemifar, S.J.; Akbarzadeh, H.; Peressi, M. First principle study of Co_2MnSi/GaAs(001) heterostructures. *J. Appl. Phys.* **2007**, *102*, 074306. [CrossRef]
31. Taylor, J.; Guo, H.; Wang, J. Ab initio modeling of quantum transport properties of molecular electronic devices. *Phys. Rev. B* **2001**, *63*, 245407. [CrossRef]
32. Waldron, D.; Haney, P.; Larade, B.; MacDonald, A.; Guo, H. Nonlinear spin current and magnetoresistance of molecular tunnel junctions. *Phys. Rev. Lett.* **2006**, *96*, 166804. [CrossRef] [PubMed]
33. Burrows, C.W.; Bastiman, S.A.; Bell, G.R. Interaction of Mn with GaAs and InSb: Incorporation, surface reconstruction and nano-cluster formation. *J. Phys. Condens. Matter* **2014**, *26*, 395006. [CrossRef] [PubMed]
34. Feng, Y.; Chen, X.; Zhou, T.; Yuan, H.K.; Chen, H. Structural stability, half-metallicity and magnetism of the CoFeMnSi/GaAs (0 0 1) interface. *Appl. Surf. Sci.* **2015**, *346*, 1–10. [CrossRef]
35. Van de Walle, C.G.; Neugebauer, J. First-principles calculations for defects and impurities: Applications to III-nitrides. *J. Appl. Phys.* **2004**, *95*, 3851. [CrossRef]